

**Evidence of Antineutrinos from Distant Reactors Using Pure Water at SNO+**

A. Allega,<sup>1</sup> M. R. Anderson,<sup>1</sup> S. Andringa,<sup>2</sup> J. Antunes,<sup>2,3</sup> M. Askins,<sup>4,5</sup> D. J. Auty,<sup>6</sup> A. Bacon,<sup>7</sup> N. Barros,<sup>2,8</sup> F. Barão,<sup>2,3</sup> R. Bayes,<sup>9</sup> E. W. Beier,<sup>7</sup> T. S. Bezerra,<sup>10</sup> A. Bialek,<sup>11,9</sup> S. D. Biller,<sup>12</sup> E. Blucher,<sup>13</sup> E. Caden,<sup>11,9</sup> E. J. Callaghan,<sup>4,5</sup> S. Cheng,<sup>1</sup> M. Chen,<sup>1</sup> B. Cleveland,<sup>11,9</sup> D. Cookman,<sup>12</sup> J. Corning,<sup>1</sup> M. A. Cox,<sup>14,2</sup> R. Dehghani,<sup>1</sup> J. Deloye,<sup>9</sup> C. Deluce,<sup>9</sup> M. M. Depatie,<sup>9,1</sup> J. Dittmer,<sup>15</sup> K. H. Dixon,<sup>16</sup> F. Di Lodovico,<sup>16</sup> E. Falk,<sup>10</sup> N. Fatemighomi,<sup>11</sup> R. Ford,<sup>11,9</sup> K. Frankiewicz,<sup>17</sup> A. Gaur,<sup>6</sup> O. I. González-Reina,<sup>18</sup> D. Gooding,<sup>17</sup> C. Grant,<sup>17</sup> J. Grove,<sup>1</sup> A. L. Hallin,<sup>6</sup> D. Hallman,<sup>9</sup> W. J. Heintzelman,<sup>7</sup> R. L. Helmer,<sup>19</sup> J. Hu,<sup>6</sup> R. Hunt-Stokes,<sup>12</sup> S. M. A. Hussain,<sup>9</sup> A. S. Inácio,<sup>2,8</sup> C. J. Jillings,<sup>11,9</sup> S. Kaluziński,<sup>1</sup> T. Kaptanoglu,<sup>4,5</sup> P. Khaghani,<sup>9</sup> H. Khan,<sup>9</sup> J. R. Klein,<sup>7</sup> L. L. Kormos,<sup>20</sup> B. Krar,<sup>1</sup> C. Kraus,<sup>9,11</sup> C. B. Krauss,<sup>6</sup> T. Kroupová,<sup>7</sup> I. Lam,<sup>1</sup> B. J. Land,<sup>7</sup> I. Lawson,<sup>11,9</sup> L. Lebanowski,<sup>7,4,5</sup> J. Lee,<sup>1</sup> C. Lefebvre,<sup>1</sup> J. Lidgard,<sup>12</sup> Y. H. Lin,<sup>9,1</sup> V. Lozza,<sup>2,8</sup> M. Luo,<sup>7</sup> A. Maio,<sup>2,8</sup> S. Manecki,<sup>11,1,9</sup> J. Maneira,<sup>2,8</sup> R. D. Martin,<sup>1</sup> N. McCauley,<sup>14</sup> A. B. McDonald,<sup>1</sup> C. Mills,<sup>10</sup> I. Morton-Blake,<sup>12</sup> S. Naugle,<sup>7</sup> L. J. Nolan,<sup>21</sup> H. M. O'Keeffe,<sup>20</sup> G. D. Orebi Gann,<sup>4,5</sup> J. Page,<sup>10</sup> W. Parker,<sup>12</sup> J. Paton,<sup>12</sup> S. J. M. Peeters,<sup>10</sup> L. Pickard,<sup>22</sup> P. Ravi,<sup>9</sup> A. Reichold,<sup>12</sup> S. Riccetto,<sup>1</sup> R. Richardson,<sup>9</sup> M. Rigan,<sup>10</sup> J. Rose,<sup>14</sup> R. Rosero,<sup>23</sup> J. Rumleskie,<sup>9</sup> I. Semeneč,<sup>1</sup> P. Skensved,<sup>1</sup> M. Smiley,<sup>4,5</sup> R. Svoboda,<sup>22</sup> B. Tam,<sup>1</sup> J. Tseng,<sup>12</sup> E. Turner,<sup>12</sup> S. Valder,<sup>10</sup> C. J. Virtue,<sup>9</sup> E. Vázquez-Jáuregui,<sup>18</sup> J. Wang,<sup>12</sup> M. Ward,<sup>1</sup> J. R. Wilson,<sup>16</sup> J. D. Wilson,<sup>6</sup> A. Wright,<sup>1</sup> J. P. Yanez,<sup>6</sup> S. Yang,<sup>6</sup> M. Yeh,<sup>23</sup> S. Yu,<sup>9</sup> Y. Zhang,<sup>6,24,25</sup> K. Zuber,<sup>15,26</sup> and A. Zummo<sup>7</sup>

(The SNO+ Collaboration)

<sup>1</sup>Department of Physics, Engineering Physics and Astronomy, Queen's University, Kingston, Ontario K7L 3N6, Canada<sup>2</sup>Laboratório de Instrumentação e Física Experimental de Partículas (LIP), Avenida Professor Gama Pinto, 2, 1649-003, Lisboa, Portugal<sup>3</sup>Universidade de Lisboa, Instituto Superior Técnico (IST), Departamento de Física, Avenida Rovisco Pais, 1049-001, Lisboa, Portugal<sup>4</sup>Department of Physics, University of California, Berkeley, California 94720, USA<sup>5</sup>Lawrence Berkeley National Laboratory, 1 Cyclotron Road, Berkeley, California 94720-8153, USA<sup>6</sup>Department of Physics, University of Alberta, 4-181 CCIS, Edmonton, Alberta T6G 2E1, Canada<sup>7</sup>Department of Physics & Astronomy, University of Pennsylvania, 209 South 33rd Street, Philadelphia, Pennsylvania 19104-6396, USA<sup>8</sup>Universidade de Lisboa, Faculdade de Ciências (FCUL), Departamento de Física, Campo Grande, Edifício C8, 1749-016, Lisboa, Portugal<sup>9</sup>School of Natural Sciences, Laurentian University, 935 Ramsey Lake Road, Sudbury, Ontario P3E 2C6, Canada<sup>10</sup>Physics & Astronomy, University of Sussex, Pevensey II, Falmer, Brighton, BN1 9QH, United Kingdom<sup>11</sup>SNOLAB, Creighton Mine #9, 1039 Regional Road 24, Sudbury, Ontario P3Y 1N2, Canada<sup>12</sup>University of Oxford, The Denys Wilkinson Building, Keble Road, Oxford, OX1 3RH, United Kingdom<sup>13</sup>The Enrico Fermi Institute and Department of Physics, The University of Chicago, Chicago, Illinois 60637, USA<sup>14</sup>Department of Physics, University of Liverpool, Liverpool L69 3BX, United Kingdom<sup>15</sup>Technische Universität Dresden, Institut für Kern und Teilchenphysik, Zellescher Weg 19, Dresden 01069, Germany<sup>16</sup>Department of Physics, King's College London, Strand Building, Strand, London WC2R 2LS, United Kingdom<sup>17</sup>Department of Physics, Boston University, 590 Commonwealth Avenue, Boston, Massachusetts 02215, USA<sup>18</sup>Universidad Nacional Autónoma de México (UNAM), Instituto de Física, Apartado Postal 20-364, México D.F. 01000, México<sup>19</sup>TRIUMF, 4004 Wesbrook Mall, Vancouver, British Columbia V6T 2A3, Canada<sup>20</sup>Physics Department, Lancaster University, Lancaster LA1 4YB, United Kingdom<sup>21</sup>School of Physics and Astronomy, Queen Mary University of London, 327 Mile End Road, London E1 4NS, United Kingdom<sup>22</sup>University of California, Davis, 1 Shields Avenue, Davis, California 95616, USA<sup>23</sup>Chemistry Department, Brookhaven National Laboratory, Building 555, P.O. Box 5000, Upton, New York 11973-500, USA<sup>24</sup>Research Center for Particle Science and Technology, Institute of Frontier and Interdisciplinary Science, Shandong University, Qingdao 266237, Shandong, China<sup>25</sup>Key Laboratory of Particle Physics and Particle Irradiation of Ministry of Education, Shandong University, Qingdao 266237, Shandong, China<sup>26</sup>MTA Atomki, 4001 Debrecen, Hungary

(Received 26 October 2022; revised 14 December 2022; accepted 20 January 2023; published 1 March 2023)

The SNO+ Collaboration reports the first evidence of reactor antineutrinos in a Cherenkov detector. The nearest nuclear reactors are located 240 km away in Ontario, Canada. This analysis uses events with energies lower than in any previous analysis with a large water Cherenkov detector. Two analytical methods are used to distinguish reactor antineutrinos from background events in 190 days of data and yield consistent evidence for antineutrinos with a combined significance of  $3.5\sigma$ .

DOI: [10.1103/PhysRevLett.130.091801](https://doi.org/10.1103/PhysRevLett.130.091801)

*Introduction.*—Measurements of reactor antineutrinos have made crucial contributions to the study of neutrinos, including the discovery of the neutrino [1] and leading measurements of neutrino oscillation parameters  $\theta_{13}$ ,  $\Delta m_{32}^2$ , and  $\Delta m_{21}^2$  [2–4]. These measurements used organic liquid scintillators to detect the products of inverse beta decays (IBDs) on protons:  $\bar{\nu}_e + p \rightarrow e^+ + n$ . The  $e^+$  carries most of the energy of the  $\bar{\nu}_e$  and produces a prompt signal, while the  $n$  is captured by a nucleus as it thermalizes, producing a delayed signal, typically of one or more  $\gamma$ 's depending on the capture isotope. Water Cherenkov detectors have used different neutrino interaction channels and also made invaluable contributions to the study of neutrinos, including the discovery of neutrino oscillations [5,6] and leading measurements of parameters  $\theta_{12}$ ,  $\theta_{23}$ , and  $\Delta m_{32}^2$  [7–11].

Previous water Cherenkov detectors have not identified reactor  $\bar{\nu}_e$ 's largely due to their detector thresholds, which have provided a low efficiency to detect the 2.2-MeV  $\gamma$  emitted when a neutron is captured by a hydrogen nucleus. One approach to improving the identification of neutrons is to make use of a higher-energy capture signal—for example, by dissolving Cl or Gd into the water [12–14]. Another approach is to attain lower thresholds, though this would also admit the more abundant radioactive backgrounds below 3 MeV [15]. Distinguishing signals and backgrounds below 3 MeV is challenging in water Cherenkov detectors due to their coarse energy resolution ( $\approx 25\%$  at 3 MeV for SNO+), which arises from small numbers of detected photons.

SNO+ has achieved the lowest energy threshold of any large Cherenkov detector, at approximately 1.4 MeV for an electron at the center of the detector, which yields an efficiency around 50% to detect the 2.2-MeV  $\gamma$  [16]. The analysis presented in this Letter addresses the higher rate of radioactivity at these lower energies using two analytical methods. Both methods suppress the accidental background from ambient radioactivity by more than 4 orders of magnitude while maintaining a relatively high IBD efficiency. All relevant backgrounds, including ( $\alpha$ ,  $n$ ) reactions and atmospheric neutrino interactions, are estimated with data in “sidebands” that are complementary to the IBD region of interest.

*Detector and data.*—SNO+ is a multipurpose neutrino experiment located at SNOLAB, 2 km underground in an active mine, near Sudbury, Ontario. The detector consists of

a spherical acrylic vessel (AV) that is 6.0 meters in radius, submerged in ultrapure water, and surrounded by an array of 9,362 eight-inch photomultiplier tubes (PMTs) at a radius of 8.5 m. From May 2017 to July 2019, the AV was filled with 905 tons of ultrapure water, and from September 2017, SNO+ operated as a low-threshold Cherenkov detector. The detector is described in Ref. [17].

Data from the SNO+ low-threshold water phase are divided into two sets: the first has higher rates of internal radioactivity due to radon ingress into the detector, while the second has significantly lower background rates owing to the installation of an  $N_2$  cover gas system on the top of the detector in September 2018. This analysis used the lower-background dataset, which has a total live time of 190.3 days. The first dataset, which has 140.7 days of live time, was analyzed to provide additional statistics in background sideband studies.

*Signal prediction.*—The rate and energy spectrum of reactor IBDs were predicted using the Huber-Mueller isotope model and other inputs, as described in Ref. [18]. The flux of  $\bar{\nu}_e$  originated from 18 reactor cores in Canada plus approximately 100 cores in the USA, with an average baseline around 620 km (baselines were weighted by the expected IBDs). The three nearest reactor complexes (Bruce, Pickering, and Darlington at distances of 240, 340, and 350 km) house Canada Deuterium Uranium (CANDU) reactors and were estimated to have yielded nearly 60% of the IBDs. The thermal powers of the CANDU reactors were modeled using hourly electrical power provided by IESO [19]. All other reactors were modeled using their respective thermal powers, provided annually as monthly averages by the IAEA [20].

Changes in the relative fractions of fissile isotopes during fuel burn-up result in a time evolution of the emitted  $\bar{\nu}_e$  energy spectrum and flux. However, because CANDU reactors are constantly refueled and  $\bar{\nu}_e$ 's were produced by a large number of reactors, the resulting variation in total flux was  $< 1\%$ . As such, constant fission fractions were used in the predictions for the CANDU pressurized heavy water reactors (PHWRs) as well as pressurized/boiling water reactors (P/BWRs): ( $^{235}\text{U}$ ,  $^{239}\text{Pu}$ ,  $^{238}\text{U}$ ,  $^{241}\text{Pu}$ ) were set to (0.52, 0.42, 0.05, 0.01) for PHWRs [21] and to (0.568, 0.297, 0.078, 0.057) for P/BWRs [22].

Known biases in the flux model were corrected by scaling the prediction by  $0.945 \pm 0.007$  to match the global average of flux measurements [23]. Because the total systematic uncertainty on the prediction is negligible

TABLE I. Initial IBD selection criteria used by the LR and BDT methods. See text for details.

|                                 | LR          |            | BDT         |           |
|---------------------------------|-------------|------------|-------------|-----------|
|                                 | Prompt      | Delayed    | Prompt      | Delayed   |
| Nhits                           | $\geq 15$   |            | $\geq 15$   | $\leq 25$ |
| $\Delta t$ ( $\mu\text{s}$ )    | (3,500)     |            | (3,500)     |           |
| ITR                             | $> 0.5$     |            | $> 0.5$     |           |
| $\beta_{14}$                    | (-0.6, 1.6) |            | (-0.6, 1.6) |           |
| $\ \mathbf{r}\ $ (internal) (m) | $< 5.7$     | $< 5.7$    | $< 5.6$     |           |
| $\ \mathbf{r}\ $ (external) (m) | (6.3, 7.5)  | (6.1, 7.6) | (6.4, 7.3)  |           |
| $z$ (external) (m)              | (-5.0, 5.0) |            | (-5.0, 5.0) |           |
| $E$ (MeV)                       | (2.5, 9.0)  | $< 4.0$    | (2.5, 9.5)  |           |
| $\Delta r$ (m)                  | $< 3.0$     |            |             |           |
| $\text{Nhits}_{p,12}$           |             |            | $> 6$       |           |

relative to the statistical uncertainties of the dataset, uncertainty components were largely taken from Ref. [18] and references therein, totaling to  $\pm 3\%$  in the rate of IBDs.

The survival probability of  $\bar{\nu}_e$ 's that reached the SNO+ detector was dominantly determined by the neutrino mass splitting  $\Delta m_{21}^2$  and oscillation angle  $\theta_{12}$ . Oscillation parameters from a recent global fit [24] were used, and the net reduction in detected IBDs due to oscillation was found to be 46%. The uncertainties in  $\Delta m_{21}^2$  and  $\sin^2 \theta_{12}$  were propagated to the expected IBD rate, resulting in a  $\pm 4\%$  uncertainty.

The expected number of IBDs within the 2.5 kton of water enclosed by the array of PMTs during the 190.3-day dataset was thus calculated to be  $160.4_{-8.4}^{+8.1}$ .

*Analysis methods.*—Two analytical methods, likelihood ratio (LR) and boosted decision tree (BDT), were used to identify coincidences of an IBD positron (“prompt” event) and neutron (“delayed” event). The two methods used a common set of criteria to remove instrumental backgrounds and electronic noise as described in Ref. [25], and then applied slightly different initial IBD selection criteria as described below and summarized in Table I.

To avoid processing the large number of events from radioactivity that were below the energy threshold, events were reconstructed only if the number of PMT hits (Nhits) was greater than or equal to 15 (roughly 2 MeV). Additionally, to ensure that neutrons could be selected, any event that followed within 1 ms of an event with  $\text{Nhits} \geq 15$  was reconstructed (the neutron capture time constant is  $207 \mu\text{s}$  [16]). The reconstruction of event position, direction, and energy, along with associated systematic uncertainties, is described in Ref. [25]. Events with poorly reconstructed energies or positions were removed using several figures of merit (FOMs). Two additional parameters were used to evaluate the compatibility of each event with a Cherenkov signal [25]. The first, in-time ratio (ITR), is the fraction of Nhits with time-of-flight-corrected hit times within

$[-2.5, 5]$  ns, which identified events with broad time distributions or poorly reconstructed positions. The second,  $\beta_{14}$ , quantifies the spatial isotropy of the hit PMTs using the first and fourth Legendre polynomials of the distribution of angles between the PMTs with respect to the reconstructed position. Events with a spatially uniform distribution of hit PMTs would have values of  $\beta_{14}$  near zero.

The reconstructed position  $\mathbf{r}$  of a prompt event was required to be in one of two fiducial volumes (FVs): inside the AV (internal) and between the AV and the PMTs (external). The region close to the AV was excluded to avoid  $(\alpha, n)$  reactions from the acrylic. This analysis is the first from SNO+ to use the external volume, where the energy scale has been calibrated as a function of event position and direction, and reconstruction systematic uncertainties have been evaluated similarly to those for the volume inside the AV.

Loose bounds were applied to the reconstructed energy  $E$  of both prompt and delayed events. The distance between prompt and delayed events  $\Delta r$  was also loosely bound. The BDT method instead used  $\text{Nhits}_{p,12}$  for delayed events, which is the maximum number of PMT hits found in a sliding time window of 12 ns, and was calculated using the time-of-flight-corrected PMT hit times assuming the prompt event position [16]. Thus, a cut on  $\text{Nhits}_{p,12}$  effectively cut on both Nhits and  $\Delta r$ , without directly relying on a reconstructed position for the delayed event. Delayed events with  $\text{Nhits}_{p,12} > 6$  were selected to suppress low-energy accidentals.

The time between prompt and delayed events  $\Delta t$  excluded the first  $3 \mu\text{s}$  after each prompt event based on one of the instrumental background criteria aimed at avoiding sequential detector triggers due to high-energy events or electronics noise. Any prompt event with more than one delayed event within  $500 \mu\text{s}$  was rejected, which reduced backgrounds that have high neutron multiplicities, such as atmospheric neutrino interactions, while sacrificing a negligible fraction of IBDs. A 100-ms veto was applied after any event with  $\text{Nhits} > 300$  (roughly 40 MeV), which reduced backgrounds from charged-current atmospheric neutrino interactions. Cosmogenic muon products were avoided by vetoing all events within 20 s after identified muons. Such a long veto window resulted in a small live-time sacrifice, since only about three muons pass through the detector every hour.

The neutron selection efficiency was measured using a deployed AmBe source [16] in order to correct for the imperfect modeling of the detector trigger around threshold. The source produces coincident pairs of a 4.4-MeV  $\gamma$  and a neutron. Events were selected with high purity, using the same criteria as in the IBD analysis. The resulting volume-weighted ratios of efficiencies (data/simulation) were applied as corrections to all predictions involving neutrons:  $0.85 \pm 0.16$  (LR) and  $0.89 \pm 0.23$  (BDT). The large uncertainties arose from the variation of the ratios



TABLE II. For the LR method, expected IBD efficiency of each initial selection, and IBD and accidental counts in 190 live days after each initial selection. The last row shows these for the final selection based on the LR cuts. Efficiencies are calculated for prompt and delayed events together. The volume-weighted correction from the AmBe source (0.85) is included in the trigger efficiency.

| Initial selection       | Efficiency (%) | IBDs  | Accidentals        |
|-------------------------|----------------|-------|--------------------|
| None                    | NA             | 160.4 |                    |
| Trigger                 | 32.9           | 52.8  |                    |
| Instrumentals [25]      | 95.7           | 50.5  |                    |
| Nhits                   | 56.9           | 28.7  |                    |
| Valid reconstruction    | 87.2           | 25.1  |                    |
| $\Delta t$              | 90.7           | 22.7  | $6.03 \times 10^6$ |
| FOMs, ITR, $\beta_{14}$ | 88.8           | 20.2  | $1.86 \times 10^6$ |
| Fiducial volume         | 50.0           | 10.1  | $5.86 \times 10^5$ |
| $E$                     | 82.1           | 8.3   | $2.61 \times 10^5$ |
| $\Delta r$              | 94.7           | 7.8   | $1.11 \times 10^4$ |
| LR selection            | 44.7           | 3.5   | 0.7                |

across the detector and the lack of complete deployment coverage across the FVs. These are the dominant uncertainties in the IBD prediction.

The total AmBe-corrected efficiency of the initial IBD selection criteria was 4.9% (LR) and 5.2% (BDT). For events that triggered the detector and satisfied the FV,  $E$ , and Nhits criteria, the initial IBD selection efficiency was about 60% for both methods. Individual selection efficiencies for the LR method are given in Table II.

After applying all initial selections, the dominant background was found to be from accidental coincidences, at an estimated rate around 58 per day, or more than  $10^4$  accidentals in the 190-day dataset. Thus, it was necessary that cuts on the LR and BDT distributions reduce the accidental rate by at least 4 orders of magnitude without sacrificing a significant fraction of the expected IBDs. The number of IBDs and accidentals is tabulated for the LR method in Table II.

The LR method constructed a likelihood ratio using probability-density histograms for reactor IBDs and accidentals. The former were generated from reactor  $\bar{\nu}_e$  simulations with SNO + RAT (a GEANT4-based [26] simulation package), and the latter were constructed by assigning a uniformly distributed random value for  $\Delta t \in [0, 1000] \mu\text{s}$  to a pair of prompt- and delayed-like events, each randomly sampled from the data after applying their respective criteria in Table I. Correlations between variables were accounted for by using two-dimensional histograms. Event energy  $E$  vs  $\beta_{14}$  accounted for the energy dependence of  $\beta_{14}$  that results from the broadening of the angular distribution of Compton-scattered  $\gamma$ 's with decreasing energy. Noting that the backgrounds have prompt  $\gamma$ 's, it also distinguished the broader angular distribution of  $\gamma$ 's from that of IBD  $e^+$ 's. A histogram of radial position  $\|\mathbf{r}\|$  vs

radial direction cosine  $\mathbf{u} \cdot \mathbf{r}$  (the unit dot product of event direction  $\mathbf{u}$  and position  $\mathbf{r}$ ) distinguished the isotropic and uniformly distributed IBDs from accidentals, which largely arose from  $\gamma$ 's emitted from the PMTs' glass, and were therefore relatively inward-pointing and at higher radii. Histograms for the  $\Delta t$  and  $\Delta r$  distributions were also included. Distinct sets of probability-density histograms were used for the internal and external volumes, and a cut on each of the two resulting LR distributions was optimized separately. Distributions of these variables are shown in Ref. [27], and more details of this method are given in Ref. [28]. The LR distribution for internal IBDs is shown as a red histogram in Fig. 1(a).

The BDT method includes several variables in addition to those used in the LR method and naturally accounts for correlations between all variables. However, the most important difference with the LR method is that it uses distinct trees for prompt and delayed events in contrast to the single likelihood ratio used in the LR method. This led to a significantly different selection of prompt-delayed pairs in the same dataset. Reactor  $\bar{\nu}_e$  simulations and accidental samples constructed from the data were used to train the BDTs. The accidental samples were constructed similarly to those of the LR method, except that  $\Delta t$  was not a parameter in either BDT. The prompt event BDT used five input variables:  $E$ ,  $\beta_{14}$ , vertical position  $z$ , transverse position  $\rho \equiv \sqrt{x^2 + y^2}$ , and radial direction cosine  $\mathbf{u} \cdot \mathbf{r}$ . A total of 12 variables were input to the delayed BDT. Similar to the LR method, the delayed BDT used  $E$ ,  $\rho$ ,  $z$ ,  $\mathbf{u} \cdot \mathbf{r}$ , and  $\Delta r$ . It also used Nhits $_{p,12}$  and its ratio to Nhits, along with five other variables that made use of the prompt event position and PMT hit information of the delayed event. The one temporal and four geometric parameters are  $T_{\text{rms}}$ ,  $N_{\text{cluster}}$ ,  $\phi_{\text{rms}}$ ,  $\theta_{\text{mean}}$ ,  $\theta_{\text{rms}}$ , and are defined in Refs. [29,30]. The delayed BDT distribution for IBDs is shown as a red histogram in Fig. 1(d).

Cuts on the LR and BDT distributions were determined by maximizing the median discovery significance presented in Ref. [31], which takes the predicted signal and background counts and background uncertainties as input. Backgrounds with delayed events from a neutron capture have fewer discriminating characteristics against IBDs, making the accidental background the most sensitive to the LR or BDT selections and therefore critical in determining their optimal cuts. Both LR and BDT methods predicted the accidental background rate using the observed rates of prompt- and delayed-like events. The accidental rate was stable across the 190-day lower-background dataset, and, after applying the optimal LR or BDT cuts, was reduced by a factor greater than  $10^4$ . The expected number of accidental coincidences was  $0.7 \pm 0.1$  for the LR method after requiring the internal (external) LR  $> 8.0$  (10.4), and  $1.4 \pm 0.1$  for the BDT method after requiring the internal (external) prompt BDT  $> 0.1$  (0.18) and the delayed BDT  $> 0.23$ . The IBD efficiencies for these cuts

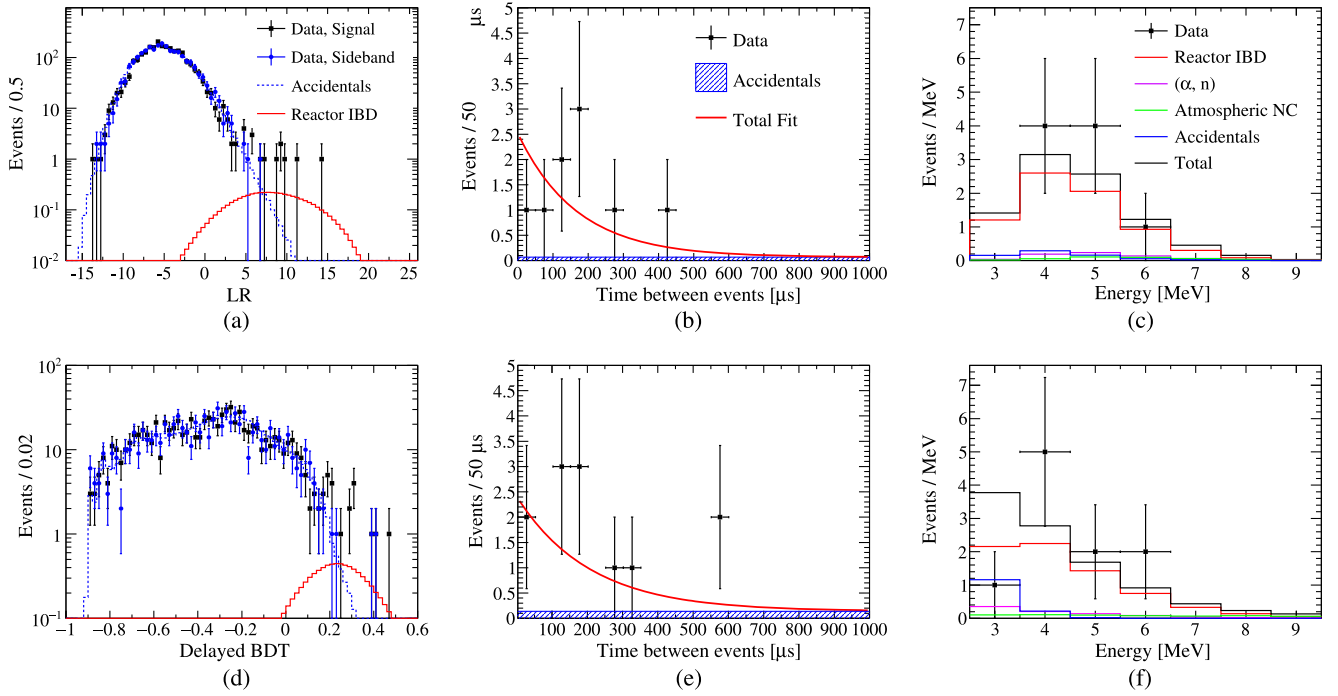


FIG. 1. The top row shows the LR method, and the bottom row shows the BDT method. Left: The LR for internal events (a) and the delayed BDT for all events (d) that pass the criteria in Table I. The signal (red) is normalized to the expectation. For both methods, there is good agreement between the data in the  $\Delta t$  sideband and the accidental estimation. Center: The  $\Delta t$  distribution for the observed events, including the region used as a sideband between 500 and 1000  $\mu\text{s}$ . The fits include exponential and flat components to model the neutron captures and accidental backgrounds, respectively. In the LR method (b), the accidental background is not expected to be flat, because  $\Delta t$  is included in the LR, but making this simplifying assumption for the fit has no significant impact [28]. Right: The prompt energy distributions for the selected events compared to the expectation for the signal and backgrounds. The background components are normalized to their expected counts, while the IBD signal is normalized to the total number of observed events minus the total number of expected background events.

were 45% and 59%, and the expected numbers of selected IBDs were  $3.5 \pm 0.7$  and  $4.8 \pm 1.4$ . These and the expected accidentals are given in Table III.

The estimates of accidental backgrounds were checked by looking at the number of coincidences in a sideband of  $\Delta t$  between 500 and 1000  $\mu\text{s}$ , keeping all other selection criteria unchanged. Figures 1(a) and 1(d) show the expected internal LR and delayed BDT distributions for IBDs and

TABLE III. Expected signal and backgrounds for LR and BDT methods in 190 live days. For BDT, only a 68% CL upper limit is given for the atmospheric  $\nu$  NC background, since no events were observed in the sideband. The sum was obtained by assuming the limit is the central value, which made the calculated significance conservative.

|               | LR            | BDT           |
|---------------|---------------|---------------|
| Reactor IBD   | $3.5 \pm 0.7$ | $4.8 \pm 1.4$ |
| Accidentals   | $0.7 \pm 0.1$ | $1.4 \pm 0.1$ |
| $(\alpha, n)$ | $0.7 \pm 0.7$ | $0.9 \pm 0.7$ |
| Atm. $\nu$ NC | $0.4 \pm 0.3$ | $< 0.6$       |
| Sum           | $5.3 \pm 1.0$ | $7.7 \pm 1.7$ |
| Observation   | 9             | 10            |

accidentals, together with the data from the signal and  $\Delta t$  sideband regions. The agreement between the sideband data and accidental expectation is very good for both methods, and the total number of accidentals that passed the final cuts in the sideband (0 and 2 for the LR and BDT methods) was consistent with the expectations of 0.7 and 1.4.

*Neutron-capture backgrounds.*—The  $(\alpha, n)$  background originates from naturally occurring  $\alpha$  decays in which the  $\alpha$  particles interact with  $^{13}\text{C}$  in the acrylic of the AV or with  $^{18}\text{O}$  in the AV and water. The  $^{13}\text{C}(\alpha, n)^{16}\text{O}$  reaction can produce deexcitation  $\gamma$ 's of up to 6.1 MeV, and the  $^{18}\text{O}(\alpha, n)^{21}\text{Ne}$  reaction produces deexcitation  $\gamma$ 's of up to 2.8 MeV. The  $^{13}\text{C}(\alpha, n)^{16}\text{O}$  reaction thus produces higher-energy prompt events, but it was highly localized to the AV, while the  $^{18}\text{O}(\alpha, n)^{21}\text{Ne}$  were distributed throughout the detector volume but produce only lower-energy prompt events. The  $(\alpha, n)$  reactions were simulated using RAT with cross sections and branching ratios from Refs. [32,33].

The rate of  $(\alpha, n)$  reactions depends directly on the rate of  $\alpha$  decays, which was dominated by  $^{210}\text{Po}$  in both the AV and the water. Predictions of the  $^{210}\text{Po}$  activity were based on radio assays of the AV and water, and they included the rate

at which  $^{210}\text{Po}$  leached into the water from the AV based on an *ex situ* leaching rate measurement. The rate of  $(\alpha, n)$  around the AV was studied in a FV sideband, using prompt events with positions around the AV in FVs complementary to the IBD FVs (see Table I). To increase the statistics of this measurement, all 331 days of live time were used. In this sideband, the LR (BDT) method observed 17 (25) events with a background of  $2.6 \pm 0.2$  ( $7.1 \pm 0.5$ ) events. In both cases, the background was dominated by accidentals, which was verified in a  $\Delta t$  sideband between 500 and 1000  $\mu\text{s}$ . The  $\Delta t$  distributions were fit with an exponential plus a constant, yielding lifetimes of  $(276 \pm 96)$   $\mu\text{s}$  and  $(183 \pm 63)$   $\mu\text{s}$ , respectively. These values are consistent with the expectation of 207  $\mu\text{s}$ . The two sideband measurements found consistent rates of  $(\alpha, n)$  reactions and were averaged to provide a single measured value. To our knowledge, this is the first identification of  $(\alpha, n)$  events in a water Cherenkov detector.

The AV sideband measurement observed a rate of  $(\alpha, n)$  events that was 4 times higher than predicted, possibly due to a smaller-than-expected rate of leaching from the AV into the water. In addition to scaling the predicted rate from the AV, a 400% uncertainty was propagated to the predicted number of  $(\alpha, n)$  interactions in the water, which was not measured directly. The impact of this large uncertainty on the total  $(\alpha, n)$  background (including both the AV and water) was relatively small, because the water component of the background has low prompt energies and is largely removed by the 2.5-MeV prompt energy criterion (see Table I). The statistical uncertainty of the AV sideband measurement dominates the uncertainty on the total  $(\alpha, n)$  background. The  $(\alpha, n)$  background expectations for the LR and BDT methods are given in Table III.

Atmospheric neutrinos can interact with oxygen nuclei, ejecting neutrons or protons, and creating excited states of  $^{15}\text{O}$  or  $^{15}\text{N}$ . The ejected nucleons can collide with nuclei and excite them or eject more nucleons. Neutral-current (NC) interactions are the dominant component of the atmospheric background, since charged-current  $\nu_\mu$  and  $\nu_e$  interactions produce high-energy leptons, which are easy to identify and reject. In NC interactions,  $^{15}\text{O}^*$  deexcites by emitting high-energy  $\gamma$ 's [34], creating a prompt signal that is followed by the capture of one or more neutrons by the hydrogen nuclei in the water.

NC atmospheric neutrino interactions produce events with observable energies above those of the IBD prompt events, primarily due to multiple deexcitation  $\gamma$ 's from more than one nucleus. These interactions also often create multiple neutrons. This background analysis used a sideband with prompt event energies between 2.5 and 25 MeV, in which events in the range of 2.5–9.5 MeV (9.5–25 MeV) were required to have a neutron multiplicity  $\geq 2$  ( $\geq 1$ ). As in the  $(\alpha, n)$  sideband analysis, all 331 days of data were used to increase statistics.

The LR method observed two events in the energy-multiplicity sideband, and the BDT method observed 0

events. A GENIE-based simulation [35] of atmospheric neutrinos was used to estimate the ratio of event rates in the sideband and signal regions, which was used to translate the sideband observations into constraints on the number of events in the signal region. Since no sideband events were observed with the BDT method, an upper limit was given at a 68% confidence level (CL). Using a ratio between the two regions eliminated uncertainties on the flux and largely on the cross section. Systematic uncertainties still arose from uncertainties on the neutron multiplicity and prompt energy distributions. These systematics were estimated by comparing the GENIE output to data from Super-Kamiokande [36] and T2K [37], yielding a 5% uncertainty in the event rate. The total uncertainty was dominated by the statistics of the sideband measurement. The atmospheric  $\nu$  background expectations for the LR and BDT methods are given in Table III.

Backgrounds from cosmogenic muons were efficiently avoided by rejecting all data within 20 s after a muon was identified. This results in no backgrounds from isotopes that undergo  $\beta$ - $n$  decay, for which the closest candidate is  $^{17}\text{N}$  [30]. With a lifetime of 4.2 s, the rate of observation was calculated to be  $< 0.01$  per year.

Geoneutrinos from  $^{238}\text{U}$  and  $^{232}\text{Th}$  decays in the Earth were predicted to produce about one quarter of the IBDs produced by reactor  $\bar{\nu}_e$ 's; however, the number of selected geo-IBDs was negligible because only a small fraction produced a prompt event with an energy above 2.5 MeV.

*Results.*—After all background sideband analyses were completed, the LR and BDT cuts were optimized as described above, and the reactor  $\bar{\nu}_e$  discovery sensitivities were thus estimated to be  $1.7\sigma$  and  $2.1\sigma$ . Then, the signal region was analyzed in the 190-day dataset, finding nine coincidences for the LR method and ten for the BDT method. The differences between the observed and expected counts were  $+3.7 \pm 3.2$  (LR) and  $+2.3 \pm 3.5$  (BDT), revealing observations greater than expectations, though not inconsistent. The total number of distinct coincidences observed by the two methods was 14, of which five were common to both. The fraction of all selected IBDs that were selected by both methods was determined with simulations to be 47%, which was supported by AmBe source data. The fraction observed in the data is approximately  $5/14 = 36\%$  (ignoring backgrounds), which is consistent with the expectation.

The events were directly inspected by fitting an exponential plus a constant to the  $\Delta t$  distributions, which yielded fitted lifetimes of  $(169 \pm 78)$   $\mu\text{s}$  and  $(207 \pm 82)$   $\mu\text{s}$  for the LR and BDT methods, respectively. These fits are shown in Figs. 1(b) and 1(e), and are consistent with the expected neutron capture time. Figures 1(c) and 1(f) show the observed prompt energy distributions, together with the expectations for the backgrounds. The selected events are distributed uniformly across the detector and across calendar time, and the delayed event energy,  $\Delta r$ , and prompt



and delayed  $\mathbf{u} \cdot \mathbf{r}$  distributions are also consistent with the simulation [27]. The 141-day higher-background dataset was also analyzed, revealing 3 and 1 coincidences for the LR and BDT methods, which are consistent with expectations of  $2.0 \pm 0.4$  and  $2.3 \pm 0.5$ .

A discovery significance of reactor  $\bar{\nu}_e$  was calculated just as the sensitivity was, except that the predicted sum of signal and background events was replaced with the observed number. The resulting significances were  $3.0\sigma$  (LR) and  $2.9\sigma$  (BDT). A combined significance was calculated in the same way, but using the total number of distinct coincidence events observed by the two methods (14) and estimating the total number of distinct background events and its uncertainty. The fraction of all background events that were selected by both methods was assumed to be the same as the fraction of IBDs—i.e., 47%. This assumption is based on the prediction that most backgrounds have a signal-like delayed event—namely, due to a neutron. The corresponding background uncertainty was conservatively estimated by assuming full correlation ( $\rho = 1$ ) between the uncertainties of the two methods, finally yielding an expectation of  $3.2 \pm 1.0$  background events. This gives a combined discovery significance of  $3.5\sigma$ . Changes in the assumptions, such as taking accidentals to have no events common to both methods, or assuming a correlation of  $\rho = 0.5$  for the background uncertainties, yielded a significance in the range of  $3.2\sigma$  to  $3.7\sigma$ .

In the absence of oscillations, the expected number of IBDs would approximately double, yielding a signal plus background around 8 and 11 events for the LR and BDT methods, respectively. As such, the current observations cannot distinguish between the oscillation and no-oscillation hypotheses.

*Conclusion.*—With a detector energy threshold around 1.4 MeV, the SNO+ Collaboration has performed the lowest-energy analysis in a large water Cherenkov detector. In a search for  $\bar{\nu}_e$  from reactors at least 240 km away, two analytical methods suppressed the accidental background by more than 4 orders of magnitude and made sideband measurements for the three relevant backgrounds. With 190 days of data, the two methods obtained consistent evidence for reactor  $\bar{\nu}_e$  and yielded a combined significance of  $3.5\sigma$ , producing the first evidence of reactor  $\bar{\nu}_e$  in a Cherenkov detector.

Capital construction funds for the SNO+ experiment were provided by the Canada Foundation for Innovation (CFI) and matching partners. This research was supported by the Natural Sciences and Engineering Research Council, the Canadian Institute for Advanced Research (CIFAR), the Queen’s University at Kingston, the Ontario Ministry of Research, Innovation and Science, the Alberta Science and Research Investments Program, the Federal Economic Development Initiative for Northern Ontario, and the Ontario Early Researcher Awards in Canada; the

Department of Energy Office of Nuclear Physics, the National Science Foundation, and the Department of Energy National Nuclear Security Administration through the Nuclear Science and Security Consortium in the U.S.; the Science and Technology Facilities Council (STFC), the European Union’s Seventh Framework Programme under the European Research Council (ERC) grant agreement, and the Marie Curie grant agreement in the United Kingdom; Fundação para a Ciência e a Tecnologia (FCT-Portugal) in Portugal; the Deutsche Forschungsgemeinschaft in Germany; DGAPA-UNAM and Consejo Nacional de Ciencia y Tecnología in Mexico; and the Discipline Construction Fund of Shandong University in China. We thank the SNO+ technical staff for their strong contributions. We would like to thank SNOLAB and its staff for support through underground space, logistical, and technical services. SNOLAB operations are supported by CFI and the Province of Ontario Ministry of Research and Innovation, with underground access provided by Vale at the Creighton mine site. This research was enabled in part by support provided by WestGRID [38] and Compute Canada [39]—in particular, computer systems and support from the University of Alberta [40] and from Simon Fraser University [41], and by the GridPP Collaboration—in particular, computer systems and support from Rutherford Appleton Laboratory [42,43]. Additional high-performance computing was provided through the “Illume” cluster funded by CFI and the Alberta Economic Development and Trade (EDT) and operated by Compute-Canada and the Savio computational cluster resource provided by the Berkeley Research Computing program at the University of California, Berkeley (supported by the UC Berkeley Chancellor, Vice Chancellor for Research, and Chief Information Officer). Additional long-term storage was provided by the Fermilab Scientific Computing Division. Fermilab is managed by the Fermi Research Alliance, LLC (FRA) under a Contract with the U.S. Department of Energy, Office of Science, Office of High Energy Physics.

- 
- [1] C. L. Cowan, F. Reines, F. B. Harrison, H. W. Kruse, and A. D. McGuire, Detection of the free neutrino: A confirmation, *Science* **124**, 103 (1956).
  - [2] D. Adey *et al.* (Daya Bay Collaboration), Measurement of the Electron Antineutrino Oscillation with 1958 Days of Operation at Daya Bay, *Phys. Rev. Lett.* **121**, 241805 (2018).
  - [3] G. Bak *et al.* (RENO Collaboration), Measurement of Reactor Antineutrino Oscillation Amplitude and Frequency at RENO, *Phys. Rev. Lett.* **121**, 201801 (2018).
  - [4] A. Gando *et al.* (KamLAND Collaboration), Reactor on-off antineutrino measurement with KamLAND, *Phys. Rev. D* **88**, 033001 (2013).

- [5] Y. Fukuda *et al.* (Super-Kamiokande Collaboration), Evidence for Oscillation of Atmospheric Neutrinos, *Phys. Rev. Lett.* **81**, 1562 (1998).
- [6] Q. R. Ahmad *et al.* (SNO Collaboration), Direct Evidence for Neutrino Flavor Transformation from Neutral-Current Interactions in the Sudbury Neutrino Observatory, *Phys. Rev. Lett.* **89**, 011301 (2002).
- [7] B. Aharmim *et al.* (SNO Collaboration), Combined analysis of all three phases of solar neutrino data from the Sudbury Neutrino Observatory, *Phys. Rev. C* **88**, 025501 (2013).
- [8] K. Abe *et al.* (Super-Kamiokande Collaboration), Solar neutrino measurements in Super-Kamiokande-IV, *Phys. Rev. D* **94**, 052010 (2016).
- [9] M. G. Aartsen *et al.* (IceCube Collaboration), Measurement of Atmospheric Neutrino Oscillations at 6–56 GeV with IceCube DeepCore, *Phys. Rev. Lett.* **120**, 071801 (2018).
- [10] K. Abe *et al.* (Super-Kamiokande Collaboration), Atmospheric neutrino oscillation analysis with external constraints in Super-Kamiokande I-IV, *Phys. Rev. D* **97**, 072001 (2018).
- [11] K. Abe *et al.* (T2K Collaboration), Publisher Correction: Constraint on the matter–antimatter symmetry-violating phase in neutrino oscillations, *Nature (London)* **580**, 339 (2020); **583**, E16 (2020).
- [12] S. N. Ahmed *et al.* (SNO Collaboration), Measurement of the Total Active B8 Solar Neutrino Flux at the Sudbury Neutrino Observatory with Enhanced Neutral Current Sensitivity, *Phys. Rev. Lett.* **92**, 181301 (2004).
- [13] K. Abe *et al.* (Super-Kamiokande Collaboration), Diffuse supernova neutrino background search at Super-Kamiokande, *Phys. Rev. D* **104**, 122002 (2021).
- [14] K. Abe *et al.* (Super-Kamiokande Collaboration), First gadolinium loading to Super-Kamiokande, *Nucl. Instrum. Methods Phys. Res., Sect. A* **1027**, 166248 (2022).
- [15] H. Watanabe *et al.* (Super-Kamiokande Collaboration), First study of neutron tagging with a water Cherenkov detector, *Astropart. Phys.* **31**, 320 (2009).
- [16] M. R. Anderson *et al.* (SNO+ Collaboration), Measurement of neutron-proton capture in the SNO+ water phase, *Phys. Rev. C* **102**, 014002 (2020).
- [17] V. Albanese *et al.* (SNO+ Collaboration), The SNO+ experiment, *J. Instrum.* **16**, P08059 (2021).
- [18] F. P. An *et al.* (Daya Bay Collaboration), Improved measurement of the reactor antineutrino flux and spectrum at Daya Bay, *Chin. Phys. C* **41**, 013002 (2017).
- [19] Independent Electricity System Operator (IESO), <https://www.ieso.ca/> (2020).
- [20] Power Reactor Information System (PRIS), <https://www.iaea.org/PRIS/> (2020).
- [21] Atomic Energy of Canada Limited (AECL), Private communication (2013), <https://www.aecl.ca/>.
- [22] K. Eguchi *et al.* (KamLAND Collaboration), First Results from KamLAND: Evidence for Reactor Antineutrino Disappearance, *Phys. Rev. Lett.* **90**, 021802 (2003).
- [23] D. Adey *et al.* (Daya Bay Collaboration), Improved measurement of the reactor antineutrino flux at Daya Bay, *Phys. Rev. D* **100**, 052004 (2019).
- [24] M. Tanabashi *et al.* (Particle Data Group), Review of particle physics, *Phys. Rev. D* **98**, 030001 (2018).
- [25] M. Anderson *et al.* (SNO+ Collaboration), Search for invisible modes of nucleon decay in water with the SNO+ detector, *Phys. Rev. D* **99**, 032008 (2019).
- [26] S. Agostinelli *et al.* (GEANT4 Collaboration), Geant4—a simulation toolkit, *Nucl. Instrum. Methods Phys. Res., Sect. A* **506**, 250 (2003).
- [27] See Supplemental Material at <http://link.aps.org/supplemental/10.1103/PhysRevLett.130.091801> for an overview of the significance calculation, and for numerical values of the events selected from data, including histograms that contain the predictions.
- [28] T. Kaptanoglu, Reactor antineutrinos in the SNO+ water phase and detector R&D for large-scale neutrino detectors, Ph.D. thesis, University of Pennsylvania, 2020, <https://repository.upenn.edu/edissertations/3889/>.
- [29] H. Zhang *et al.* (Super-Kamiokande Collaboration), Supernova Relic Neutrino search with neutron tagging at Super-Kamiokande-IV, *Astropart. Phys.* **60**, 41 (2015).
- [30] Y. Zhang *et al.* (Super-Kamiokande Collaboration), First measurement of radioactive isotope production through cosmic-ray muon spallation in Super-Kamiokande IV, *Phys. Rev. D* **93**, 012004 (2016).
- [31] G. Cowan, Discovery sensitivity for a counting experiment with background uncertainty, <https://www.pp.rhul.ac.uk/~cowan/stat/medsig/medsigNote.pdf> (2012), last accessed in April 2022.
- [32] T. Murata *et al.*, Evaluation of the ( $\alpha$ , xn) reaction data for JENDL/AN-2005 (2006), <https://www.wndc.jaea.go.jp/ftpnd/jendl/jendl-an-2005.html>.
- [33] NNDC, Nudat 3.0, <https://www.nndc.bnl.gov/nudat3/> (2022).
- [34] H. Ejiri, Nuclear deexcitations of nucleon holes associated with nucleon decays in nuclei, *Phys. Rev. C* **48**, 1442 (1993).
- [35] C. Andreopoulos *et al.*, The GENIE neutrino Monte Carlo generator, *Nucl. Instrum. Methods Phys. Res., Sect. A* **614**, 87 (2010).
- [36] L. Wan *et al.* (Super-Kamiokande Collaboration), Measurement of the neutrino-oxygen neutral-current quasielastic cross section using atmospheric neutrinos at Super-Kamiokande, *Phys. Rev. D* **99**, 032005 (2019).
- [37] K. Abe *et al.* (T2K Collaboration), Measurement of neutrino and antineutrino neutral-current quasielasticlike interactions on oxygen by detecting nuclear deexcitation  $\gamma$  rays, *Phys. Rev. D* **100**, 112009 (2019).
- [38] <https://www.westgrid.ca>.
- [39] <https://www.computecanada.ca>.
- [40] <https://www.ualberta.ca>.
- [41] <https://www.sfu.ca>.
- [42] P. J. W. Faulkner *et al.* (GridPP Collaboration), GridPP: development of the UK computing Grid for particle physics, *J. Phys. G* **32**, N1 (2006).
- [43] D. Britton *et al.*, GridPP: the UK grid for particle physics, *Phil. Trans. R. Soc. A* **367**, 2447 (2009).